Inflammation Research

ORIGINAL ARTICLE

A new mouse unilateral model of diffuse alveolar damage of the lung

A. S. Chernov[1] · A. A. Minakov[1] · V. A. Kazakov[1] · M. V. Rodionov[1,4] · I. N. Rybalkin[5] · T. N. Vlasik[5] · D. V. Yashin[2] ·
L. P. Saschenko[2] · A. A. Kudriaeva[1] · A. A. Belogurov[1] · I. V. Smirnov[1] · S. Ya. Loginova[3] · V. N. Schukina[3] ·
S. V. Savenko[3] · S. V. Borisevich[3] · K. A. Zykov[5,6,7] 🅾 · A. G. Gabibov[1] · G. B. Telegin[1]

Abstract

Objective and design The existing biological models of diffuse alveolar damage (DAD) in mice have many shortcomings. To offset these shortcomings, we have proposed a simple, nonsurgical, and reproducible method of unilateral total damage of the left lung in ICR mice. This model is based on the intrabronchial administration of a mixture of bacterial lipopolysaccharide (LPS) from the cell wall of S. enterica and α-galactosylceramide (inducing substances) to the left lung.

Methods Using computer tomography of the lungs with endobronchial administration of contrast material, we have been able to perform an operative intravital verification of the targeted delivery of the inducer. The model presented is characterized by more serious and homogeneous damage of the affected lung compared to the existing models of focal pneumonia; at the same time, our model is characterized by longer animal survival since the right lung remains intact.

Results The model is also characterized by diffuse alveolar damage of the left lung, animal survival of 100%, abrupt increases in plasma levels of TNFa, INFg, and IL-6, and significant myocardial overload in the right heart. It can be used to assess the efficacy of innovative drugs for the treatment of DAD and ARDS as the clinical manifestations that are developed in patients infected with SARS-CoV-2. Morphological patterns of lungs in the noninfectious ("sterile") model of DAD induced by LPS simultaneously with α-galactosylceramide (presented here) and in the infectious model of DAD induced by SARS-CoV-2 have been compared.

Conclusion The DAD model we have proposed can be widely used for studying the efficacy of candidate molecules for the treatment of infectious respiratory diseases, such as viral pneumonias of different etiology, including SARS-CoV-2.

Keywords Mouse model · Lung · Acute respiratory distress syndrome · Diffuse alveolar damage · COVID-19

✉ K. A. Zykov
   kirillaz@inbox.ru

1   Shemyakin-Ovchinnikov Institute of Bioorganic Chemistry
    of the Russian Academy of Sciences, Pushchino, Russia

2   Institute of Gene Biology, Russian Academy of Sciences,
    Moscow, Russia

3   48Th Central Scientific Research Institute, Ministry
    of Defense of the Russian Federation, Moscow, Russia

4   Medical Radiological Research Center (MRRC) named
    after A.F. Tsyb—Branch of the National Medical

    Radiological Research Center of the Ministry of Health
    of the Russian Federation, Moscow, Russia

5   Federal State Budgetary Institution National Medical
    Research Center of Cardiology, Ministry of Health
    of the Russian Federation, Moscow, Russia

6   FGBU "Research Institute of Pulmonology" under FMBA
    of Russia, Moscow, Russia

7   FSBEI HE A.I.Evdokimov MSMSU MOH Russia, Moscow,
    Russia

Introduction

Currently, the treatment of severe COVID-19, which is accompanied by the development of acute respiratory distress syndrome (ARDS), continues to be a challenge. A comprehensive research of possible clinical pharmacological approaches requires the use of animal models of ARDS for evaluating the efficacy of the proposed solutions. The pathomorphological basis of ARDS is a diffuse alveolar damage (DAD) of the lungs, leading to severe respiratory failure due to diffuse damage to the alveolar capillary membranes. DAD is characterized by excessive production of pro-inflammatory cytokines and chemokines, massive infiltration of neutrophils to the lungs, endothelial dysfunction, microthromboses, interstitial and alveolar edema, death of alveolar epithelial cells, and activation of macrophages [1]. DAD is a relatively nonspecific reaction and may be associated not only with severe COVID-19 but with other viral and bacterial pneumonias, sepsis, severe injury, or aspiration of gastric contents [2–4]. Moreover, DAD may cause bilateral noncardiac respiratory failure [5].

Currently, all existing biological models of DAD-ARDS are seriously limited, since they do not account for some concurrent factors, such as age, chronic medical conditions, and environmental effects [6, 7]. Nevertheless, animal models have substantially contributed to understanding some mechanisms responsible for the development of lung damage in ARDS [8–10]. Also, despite the fact that this syndrome had been described back in 1967 [11], assessment of the impacts of focal inflammatory heterogeneity in acute lung damage using animal biological models remains difficult [10, 12].

There exist different animal models that can be used for studying the mechanisms of acute lung damage [13]. Most of them are based on administration to animals of different agents or interventions capable of inducing DAD (LPS, lipid embolism, acid aspiration, ischemia–reperfusion of lung and distal vessels). One of the most common models of DAD consists of the induction of damage by intratracheal administration of α-galactosylceramide 24 h before the injection of lipopolysaccharide [14, 15]. This model is characterized by high lethality and by the requirement for dual intubation of the trachea under general anesthesia. Also, intratracheal administration of LPS causes focal damage in the lungs [13, 14, 16, 17]. Another promising approach is a mouse model that involves the delivery of a damaging agent (0.1 N HCl mixed with a radioactive label) into one lobe of the right lung, which substantially increases the survival of experimental mice as compared to the bilateral instillation of 0.1 N HCl [18]. However, hydrochloric acid as an inducer of inflammation has a narrow specificity and cannot be used for modeling the damage caused by microbiological agents.

To be applicable for long-term follow-up studies, the DAD model should possess a relatively low invasiveness. At the same time, one should be confident that the entire volume of the lung has been exposed during the experiment and the therapeutic agent reaches the damaged areas [19, 20]. Heart and lungs are combined pathophysiologically in a single cardiopulmonary continuum, and the pathophysiological process in the lungs can have some impact on the cardiovascular system. We believe that another obvious disadvantage of DAD models described in the literature is the lack of data regarding changes to the functional morphology of the myocardium, of the right heart in particular.

To overcome these issues and take into consideration the urgent need for the development of animal DAD models to evaluate the effectiveness of potential therapies not only during the acute phase of SARS-CoV-2 infection but also during the recovery of the respiratory apparatus after COVID- 19, we used an optimized, low-invasive, unilateral mouse model of DAD with an intratracheal injection of α-galactosylceramide (GC) simultaneously with lipopolysaccharide. The aim of this study was to characterize immunological and morphological features of the optimized low invasive mouse model of acute unilateral diffuse lung damage, and to compare morphological features of the proposed LPS and GS-induced model of DAD with those of the infectious model of DAD induced by SARS-CoV-2.

Materials and methods

Animals and the scheme of DAD modeling in mice induced by LPS simultaneously with GC (noninfectious model)

Mice with an average weight ($\pm$ SEM) of 40.1 ($\pm$ 1.85) g were used. All animals were housed under standard conditions in the Animal Breeding Facility of BIBCh, RAS (the Unique Research Unit Bio-Model of the IBCh, RAS; the Bioresource Collection—Collection of SPF-Laboratory Rodents for Fundamental, Biomedical and Pharmacological Studies), which has an international accreditation AAALACi. All experiments and manipulations were approved by the institutional animal care and use committee (IACUC No. 746/20 from 20/04/20). All procedures with animals were performed according to primary standards of AAALACi: the Guide for the Care and Use of Laboratory Animals (Guide), NRC, 2011 and the European Convention for the Protection of Vertebrate Animals Used for Experimental and Other Scientific Purposes, Council of Europe (ETS 123).

DAD was induced by a single instillation into the left lung of the inducing mixture consisting of 100 μl (1 mg/ml) LPS from Salmonella enterica (MilliporeSigma, USA) and 100 μl (50 μg/ml) α-galactosylceramide (Avanti Polar

Lipids, USA). The trachea was intubated with an intravenous catheter 20G that was put forward into the left mainstem bronchus, with the animal lying in the lateral position. As premedication during the intubation of the trachea, a short-acting hypnotic agent Propofol was used (Hana Pharmaceutical, Co. Ltd., Republic of Korea). The hypnotic agent was administered as an intravenous bolus into the lateral tail vein at a dose of 20 mg/kg. The animals were randomly assigned to two treatment groups with ten animals in each group ($n = 20$): Group 1—control, intact animals; Group 2—induction of DAD in animals which simultaneously received 200 µl of physiological saline. The animals were followed up for 3, 5, 7, 14, 30, 45, and 60 d.

Control of targeted delivery of the compounds, and evaluation of the extent of lung damage

CT scanner MRS*CT/PET (MR Solution, UK) were used to control the degree of filling of the lungs, produce the images and evaluate the extent of lung damage. Scan parameters: energy 40 kVp, exposure 100 ms, current 1 mA, stepping angle 1°. During the imaging, the animals were anesthetized with a 3% mixture of isoflurane and air, and maintained in a specialized bed at a temperature of $+37$ °C. The CT images obtained were processed using the VivoQuant software (Invicro, UK). At a preliminary stage, uniformity of the inducer along the bronchial tree was assessed using contrast bronchography and an iodinated contrast agent Omnipak (GE Healthcare AS, Norway).

The lung volume and the average density of left (experimental) and right (control) lung tissues were measured after segmentation of these lobes either in the automatic mode (using -300 to -800 Hounsfield units as the cutoff density) or manually. The volume was expressed in mm3 and the density in Hounsfield units (HU ± SEM).

The assay of chemokines and cytokines

Blood from individual animals was collected at 3, 10 and 24 h after DAD induction into EDTA tubes to obtain plasma. Bio-Plex Pro Mouse Cytokine Panel 33-Plex (BIO-RAD, USA) was used to measure the levels of chemokines and cytokines in plasma. Plasma samples diluted at 1:3 (50 µl) were incubated with magnetic beads, washed up, and then incubated with detecting antibodies and SA-PE. The data were obtained using Luminex 200 analyzer and analyzed using the xPONENT software.

Infection of mice with SARS-CoV-2

To obtain the infectious model of DAD induced by SARS-CoV-2, we infected the humanized mice C57BL/6J-TgTn (CAG-humanACE2-IRES-Luciferase-WPRE-polyA) by intranasal injection of SARS-CoV-2 at 105 PFU and 106 PFU in 40 µl of saline. Transgenic mice were obtained from the animal breeding facility of BIBCh, RAS (the Unique Research Unit Bio-Model of the BIBCh, RAS; the Bioresource Collection—Collection of SPF-Laboratory Rodents for Fundamental, Biomedical, and Pharmacological Studies). The experiments were conducted under the conditions of a specialized BSL-3 laboratory (Sergiev Posad). In the mice that died during the follow-up period, the levels of SARS-CoV-2 accumulation in the lungs were assessed based on the formation of negative colonies (PFU) in the cultured Vero Cl008 cells [21]. After a two-week inactivation period in 10% formalin solution, the lungs were subjected to histological examination.

Measurement of respiration

Respiratory parameters were assessed using an 8-channel base module PowerLab 8/35 (PL3508) ADInstruments Pty Ltd. (Australia) equipped with spirometer unit (FE141) and Respiratory Flow Head (MLT1L) on study days 7, 14, 30 and 45. An animal was immobilized in a fixer house and allowed to stand for at least 2 min, so that it could calm down and take a convenient posture. A breathing mask fixed on the entry of respiratory flow head was tightly pressed to the animal's nose. After a clearly distinguishable signal, a recording function in LabChart7 software was turned on. Parameters studied: frequency of respiratory movements (respiratory rate), breaths per minute; peak expiratory flow (PEF), ml/sec; respiratory volume (tidal volume), ml. Minute respiratory volume was calculated independently (frequency of respiratory movements × respiratory volume).

Histological examination

The heart and lungs, filled with 10% solution of neutral formalin, were subjected to further dissection after a satisfactory fixation: a tissue fragment was taken from each lobe of the lung (1—from the left lobe, 4—from right lobes); a sagittal section of the heart permitted visualization of all the heart chambers. Tissue samples were washed in running water, dehydrated in ethanol solutions of increasing concentrations, and embedded in paraffin. Paraffin sections of 4–5 µm width stained with hematoxylin and eosin were examined according to the Mallory method using standard light microscopy on an AxioScope.A1 microscope (Carl Zeiss, Germany). The microphotographs of histological preparations were obtained using a high-resolution camera Axiocam 305 color (Carl Zeiss, Germany) and ZEN 2.6 lite software (Carl Zeiss, Germany). When studying functional morphology of the lungs in the short-term (day 3), medium-term (days 5–7), and long-term (days 14–60), particular attention was given to evaluation of the time course of the

following pathomorphological parameters: the presence and prevalence of peribronchial and perivascular inflammatory cell infiltration, the presence of immunocompetent cells in the interalveolar septa and in the lumen of pulmonary acini, the presence of sites of collapsed lung tissue, transudate in the lumen of alveoli, foci of necrosis, and perivascular, peribronchial, and interstitial fibrosis in the outcome of the inflammatory process. In the heart, a particular attention was given to the state of myocardium of the right ventricle and right atrium, dilation of the right ventricle and right atrium as potential markers of pulmonary hypertension in the setting of total and subtotal atelectasis of the left lobe of the lungs. On the microphotographs of histological preparations from the control age-matched animals and from mice with DAD, diameters of cardiomyocytes of the right and left ventricle were measured to obtain the quantitative assessment of changing workloads on the heart.

For comparative evaluation of the severity of pathohistological findings in noninfectious and infectious models, all characteristics were evaluated by one morphologist semi-quantitatively on a three-point scale ranging from the absence of a sign to its maximum severity.

Results

Structural features of the model of acute total lung damage

We have developed a simple and low-invasive method of damaging one lung in mice. Intubation of the left mainstem bronchus in mice was performed using an intravenous catheter as described above. The mandatory condition of successful intubation for DAD modeling is placing an animal in the lateral position. On day 3 after intubation, the animals were euthanized and the cardiopulmonary complex was dissected and examined.

As compared to lungs of intact mice (Fig. 1A (i)), left lungs of experimental mice were totally damaged (Fig. 1A (ii)), with air volume lacking due to atelectasis development. To control the targeted delivery of the inducer into the lung, an approach with contrast agent Omnipak was applied. Fifteen minutes after the injection of the inducer mixed with contrast agent, mice were subjected to the antemortem CT. CT images showed that induction of DAD is entirely unilateral, with no involvement of the right lobes of the lung in the inflammatory process (Fig. 1A(iii)). Figure 1A (iv) shows the 3D-reconstruction of CT images using VivoQuant software.

Fig. 1 Characterization of the DAD model in ICR mice. **A** macroscopic samples of the mouse lungs: (i) intact lungs as part of the complex of organs; (ii) total damage of the left lung after intrabronchial administration of LPS + GC mixture; (iii) CT control of targeted delivery of the inducer using the contrast agent Omnipak; (iv) 3D-reconstruction of the damaged left lung of the mouse. **B** morphological pattern and CT images of mouse lungs (both intact and after DAD induction) on days 7, 14, 30, and 60
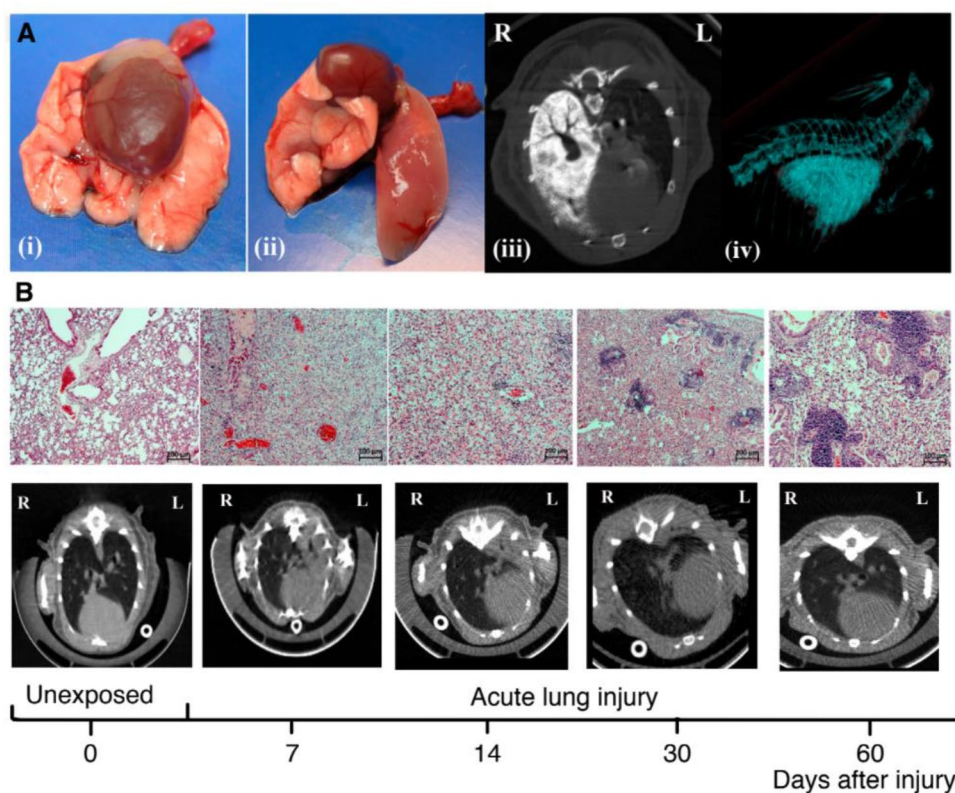
Morphological findings in the lungs of ICR mice with DAD induced by LPS simultaneously with GC (noninfectious model)

Morphological changes in the lung tissue of experimental mice with DAD were assessed on days 3, 5, 7, 14, 30, and 60. Figure 1B shows the histological pattern and CT image of the intact lung. On day 3, the left lobes of lungs from DAD mice showed total collapse of the lung tissue with a pattern of diffuse alveolar damage of the elements of the blood–air barrier: the walls and the lumen of alveoli were consistently infiltrated with numerous segmented neutrophils and few macrophages. The presence of transudate was observed along the entire lumen of alveoli, sometimes with small air bubbles. A moderate focal perivascular and peribronchial infiltration, mostly with segmented neutrophils and sparse lymphocytes and mononuclear cells, was also observed. The lumen of most bronchi (large in particular) was completely obturated with desquamated cells of respiratory epithelium, numerous segmented leukocytes, and single mononuclear cells. A marked congestion and stasis of red blood cells in the microcirculatory vessels in the setting of general diffuse congestion in the left lobe vessels has been reported. The described ventilation–perfusion disorders (total atelectasis of the left lobe combined with slowing of blood flow and congestion of microcirculatory vessels) may be regarded as the first phase of ARDS associated with coronavirus infection [15, 22–24].

By day 5 of the follow-up, the fraction of mononuclear cells was substantially increased in the perivascular and peribronchial infiltrate, as well as in the walls and lumen of the pulmonary acini. The alveolar lumen was still filled with transudate, the bronchi were totally obturated, and the left lobe was completely cut off from gas exchange.

By day 7, the overall pattern of focal perivascular and peribronchial infiltrate and that of diffuse infiltration of the walls and lumen of the alveoli were characterized by the predominance of mononuclear cells (Fig. 1B). The left lobe of the lung was still not involved in gas exchange (Fig. 1B); diffuse congestion of vessels was reported.

By day 14, some bronchi in the left lobe of DAD mice were partially or completely patent; hypoventilation sites of pulmonary acini in different lobe segments appeared (Fig. 1B). Omnipresent focal peribronchial and progressive perivascular mononuclear infiltration were observed, as well as infiltration of the widened walls and the narrowed lumen of alveoli with mononuclear cells (Fig. 1B).

By day 30, the extent of involvement of the left lobe in overall gas exchange progressively increased, however, the diffuse mononuclear infiltration of the walls and lumen of alveoli, and focal perivascular and peribronchial mononuclear infiltration was still present (Fig. 1B). It is also noteworthy that by day 30, the left lobe of the lungs has not restored air volume in any of the animals: overall volume of pulmonary tissue was reduced, interalveolar septa widened, and perivascular and peribronchial spaces were slightly widened due to fibrotic changes (Fig. 1B). In most samples, sites of rupture of interalveolar septa were observed by day 30.

By day 45 of the follow-up, a further increase in the gas exchange in the left lobe of the lung was observed; however, its original size was not reached—the left lung volume remaining reduced by at least 50–60% from baseline. Mononuclear infiltration of various severities was present in the walls and lumen of alveoli of the majority of the lobe; however, portions of pulmonary tissue free from mononuclear infiltration also appeared. A marked peribronchial and perivascular mononuclear infiltration was observed.

The same pattern was observed on day 60 of the follow-up (from the day of administration of LPS + GC mixture); even after such a long period of time, mononuclear cells were present in abundance in perivascular and peribronchial spaces, as well as in most parts of the walls and lumen of pulmonary acini (Fig. 1B). No relevant morphological changes in the right lobes of the lungs were observed from day 3 to day 60 of the follow-up. The pulmonary tissue was almost intact, with obvious signs of compensatory ventilation.
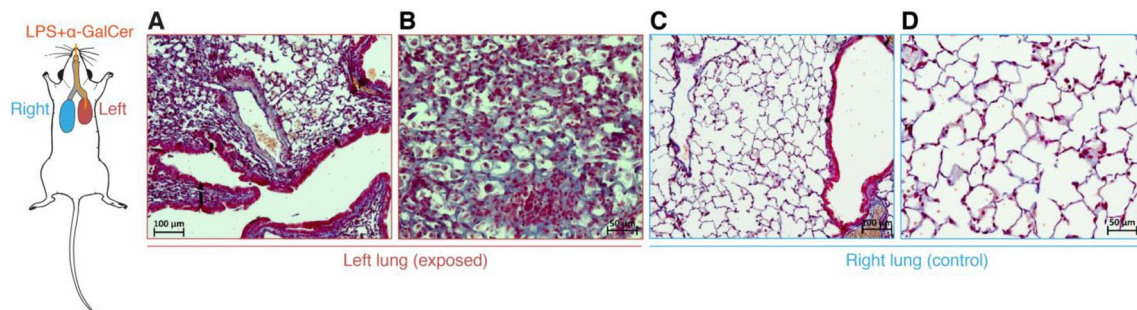

Fig. 2 Fragments of left (left column) and right (right column) lobes of the lung of male ICR mice in the DAD model on day 60 of the follow-up: moderate perivascular and peribronchial fibrotic changes (**A**), and widening of the alveolar walls in the left lobe (**C**) as compared to intact lobes of the right lung (**B**, **D**). Mallory staining. Magnification: 100x (**A**, **B**) and 200x (**C**, **D**)

When studying functional morphology of the lungs in the long-term follow-up periods on histological preparations stained according to the Mallory method, a moderate perivascular and peribronchial fibrosis was observed, and there was a widening of interalveolar septa due to fibrotic changes in pulmonary acini. On days 30 and 45, fibrotic changes were subtle, and collagen fibers were thin and immature. The final pattern of fibrotic changes became evident by day 60 of the follow-up, by which time the definitive maturation of collagen fibers in perivascular and peribronchial spaces was observed (Fig. 2A) and fibrotic changes appeared in markedly widened walls of pulmonary acini (Fig. 2C).

In some animals (not more than 10% of the total number), small foci of necrosis were found, with subsequent mononuclear infiltration on day 7 of the follow-up (Fig. 3A) and signs of organization by day 14 (Fig. 3B). By day 7, dilation of cavities and thinning of the myocardial wall of the right ventricle and right atrium were observed in some animals (not more than 30% of the total number). The changes in the myocardium described above indirectly indicate a volume overload of the right heart and pulmonary hypertension. These findings were supported by quantitative parameters of functional morphology of the myocardium directly associated with the load on the heart muscle, such as the diameter of cardiomyocytes of the left and, particularly, of the right ventricles. Indeed, diameters of cardiomyocytes of right and left ventricles of intact 6-month male ICR mice were 11.2 ± 1.2 and 13.1 ± 1.4 μm, respectively. On day 7 after the unilateral intrabronchial administration of the GC + LPS mixture, there were no significant changes in the diameters of cardiomyocytes of the right and left ventricles (11.8 ± 0.9 and 14.6 ± 1.1 μm, respectively). On day 30, a hypertrophy of cardiomyocytes of both the right (14.1 ± 0.8 μm) and left (15.2 ± 0.7 μm) ventricles was observed, and already by the end of the second month after induction of acute diffuse lung damage, in the setting of fibrotic changes of the pulmonary

Table 1 Mean spirometry values

Testing day	Respiratory rate, breaths per minute	Respiratory volume, ml	Peak expiratory flow, ml/sec
	Mean ± SD	Mean ± SD	Mean ± SD
Intact animals			
Day 7	195 ± 9.1	0.608 ± 0.020	7.32 ± 0.17
Day 14	203 ± 7.0	0.605 ± 0.016	7.20 ± 0.28
Day 30	201 ± 10.1	0.629 ± 0.013	7.22 ± 0.32
Day 45	197 ± 7.8	0.603 ± 0.020	7.40 ± 0.44
Animals with DAD			
Day 7	$347 \pm 15.3^*$	$0.260 \pm 0.006^*$	$3.45 \pm 0.20^*$
Day 14	$328 \pm 12.9^*$	$0.347 \pm 0.019^*$	$4.47 \pm 0.35^*$
Day 30	$270 \pm 26.9^*$	$0.449 \pm 0.023^*$	6.27 ± 0.07
Day 45	218 ± 12.7	0.572 ± 0.039	6.96 ± 0.13

*—$p \leq 0.05$ as compared to group 1 without modeling, Mann–Whitney paired comparison test

parenchyma, the diameter of cardiomyocytes of the right and left ventricles reached 16.8 ± 1.1 and 17.6 ± 1.2 μm, respectively.

Study of functional changes in the respiratory system

Mean values of respiratory parameters are shown in Table 1. During the assessment of respiratory movements frequency (per minute), the following significant differences were found. On observation days 7, 14 and 30, frequency of respiratory movements in animals from model DAD group significantly differed from that in control animals indicating the successful modeling of diffuse alveolar damage values in the lungs. On study day 45, there were no significant differences in respiratory rate between animals from model DAD group and those from control group.
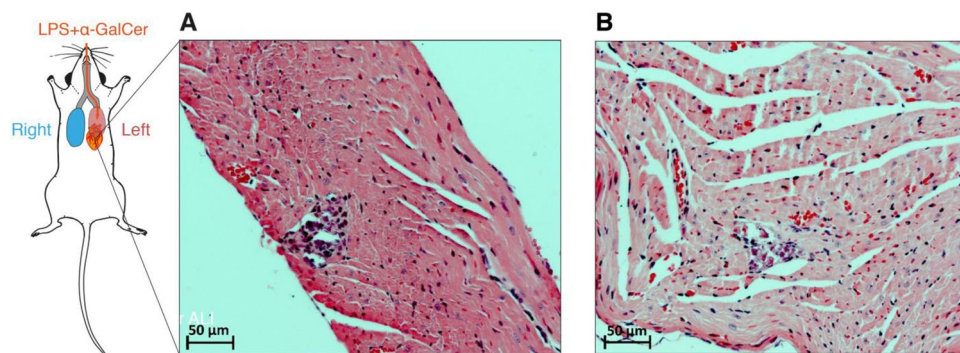

Fig. 3 Fragments of myocardium of the right ventricle of male ICR mice in the DAD model on days 7 (**A**) and 14 (**B**) of the follow-up: small foci of necrosis of cardiomyocytes at stages of mononuclear infiltration (on the left) and organization (on the right) as indirect signs of volume overload of the right heart, and pulmonary hypertension. Staining with hematoxylin and eosin. Magnification: 200x

Similar results have been obtained in the analysis of respiratory volume (Table 1). In the analysis of peak expiratory flow, the following differences have been reported. On study days 7 and 14, the animals from model DAD group significantly differed from those from control group, indicating the successful modeling of diffuse alveolar damage in the lungs. On study days 30 and 45, there were no significant differences in peak expiratory flow between the animals from model DAD group and those from control group.

The functional tests have shown that in acute and subacute periods of DAD, a rise in respiratory rate, and a decrease in respiratory volume and peak expiratory flow take place. These data concord well with clinical manifestations of ARDS in humans, including those with coronavirus inection [41, 42].

Model verification by imaging

A dynamic assessment of the volume of pulmonary lobes and its average density in Hounsfield units was performed using a CT scanner MRS*CT/PET. The results are shown in Fig. 4.

One day after induction of DAD, both the volume and density of the two lungs remained at baseline levels. On day 7 of the study, a twofold decrease in the volume of the left lung (from 417 ± 37 to 273 ± 41 mm^3) was reported, and its density in Hounsfield units significantly increased (from -466 ± 97 to -104 ± 79 HU). The parameters of the right lung corresponded to the control. By day 14, the volume of the right lung increased to 1002 ± 102 mm^3, with no change in density. At the same time, the volume of the left lung remained unchanged (264 ± 41 mm^3) and its density decreased to -189 ± 22 HU. Further observations have shown that by days 30–60, both lungs tended to recover;
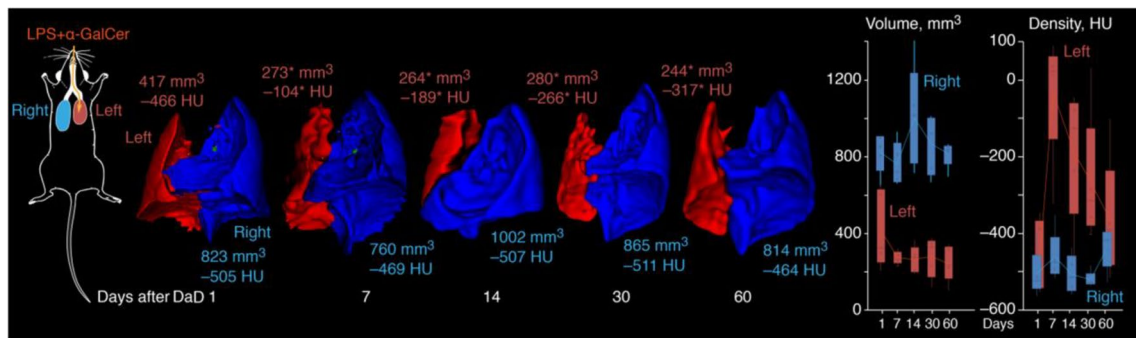

Fig. 4 Dynamic characterization of changes in the volume and density of the lungs in mice with DAD (*$P < 0.05$)
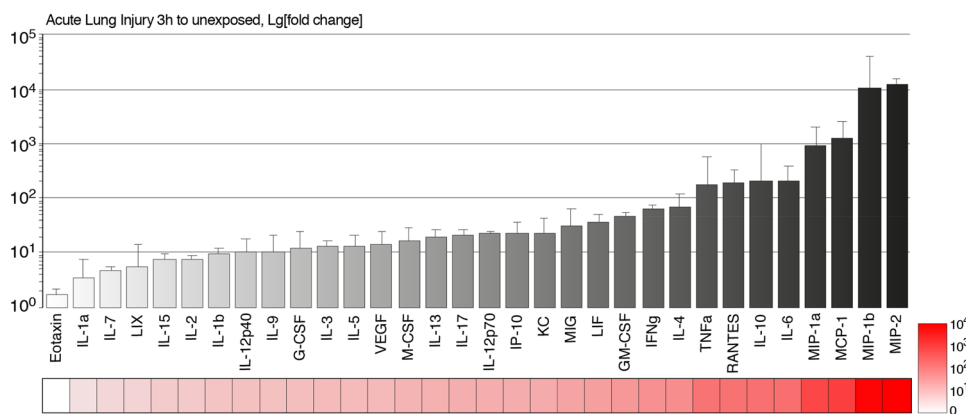

Fig. 5 Level of plasma cytokines in mice with DAD 3 h after syndrome induction, in comparison with unexposed animals. Bars represent averages with standard deviations. Granulocyte colony-stimulating factor (G-CSF), liposaccharide-induced CXC chemokine (LIX/CXCL5), vascular endothelial growth factor (VEGF), granulocyte–macrophage colony-stimulating factor (GM-CSF), keratinocyte chemoattractant (KC), leukemia inhibitory factor (LIF), macrophage colony-stimulating factor (M-CSF), monokine induced by gamma (MIG/CXCL9), tumor necrosis factor (TNF), interferon gamma (IFNg), RANTES (CCL5), interferon g-induced protein 10 kDa (IP-10/CXCL10), monocyte chemoattractant protein 1 (MCP-1/CCL2), and macrophage inflammatory proteins (MIP)—MIP-1a, MIP-1b, and MIP2

however, the left lobe still remained reduced compared to baseline.

Measuring the levels of cytokines and chemokines

We then measured cytokine profiles in mice with induced DAD (Fig. 5). Our data suggest that during the first 3 h almost all cytokines and chemokines were dramatically elevated in the plasma of mice with induced DAD. Levels of the Eotaxin, granulocyte colony-stimulating factor (G-CSF), IL-1a, IL-1b, IL-2, IL-3, IL-5, IL-7, IL-9, IL-12p40, IL-15, liposaccharide-induced CXC chemokine (LIX/CXCL5), and vascular endothelial growth factor (VEGF) were increased up to 10 times, whereas levels of the granulocyte–macrophage colony-stimulating factor (GMCSF), IL-4, IL-12p70, IL-13, IL-17, keratinocyte chemoattractant (KC), leukemia inhibitory factor (LIF), macrophage colony-stimulating factor (M-CSF), and monokine induced by gamma (MIG/CXCL9) were upregulated by up to two orders of magnitude in comparison with unexposed animals. Levels of the classical pro-inflammatory cytokines released during ARDS, namely tumor necrosis factor (TNF), interferon IFNg, and IL-6, were increased by approximately two orders of magnitude. Importantly, serum levels of chemokines RANTES (CCL5), interferon ɣ-induced protein 10 kDa (IP-10/CXCL10), monocyte chemoattractant protein 1 (MCP-1/CCL2), and macrophage inflammatory proteins (MIP)—MIP-1a, MIP-1b, and MIP2 were dramatically upregulated in mice with DAD, and concentration of the last four chemokines increased from 1 000 to 10 000 times.

Morphological findings in the lungs of male hACE2 mice infected with SARS-CoV-2 (infectious model)

The infection of male hACE2 mice was instigated by intranasal administration of the virus SARS-CoV-2. In the groups of animals that received the virus in high infective doses ($n = 14$), two animals died on day 3 and 12 animals died on day 4. In the lungs of mice that died from a high dose of the virus, the key morphological findings were the formation of hyalin-like membranes (Fig. 6A) and acute disorder of microcirculation (Fig. 6B) in the form of congestion, stasis, blood sludge, and microthromboses, as well as severe congestion of large vessels (so called "shock lung"). The findings described were observed in all animals. More rarely (in 40–60% cases), tissue detritus (Fig. 6C) and transudate (Fig. 6D) were present in the lumen of acini. In single animals, there were sparse mononuclear cells in the lumen and wall of alveoli (Fig. 6E) and single segmented neutrophils in the interalveolar septa (Fig. 6F).

Comparison of the morphological features in infectious and noninfectious mouse models

A comparison of the morphological characteristics of lung lesions in an infectious and noninfectious mouse model is shown in Table 2. The table shows only the early (before day
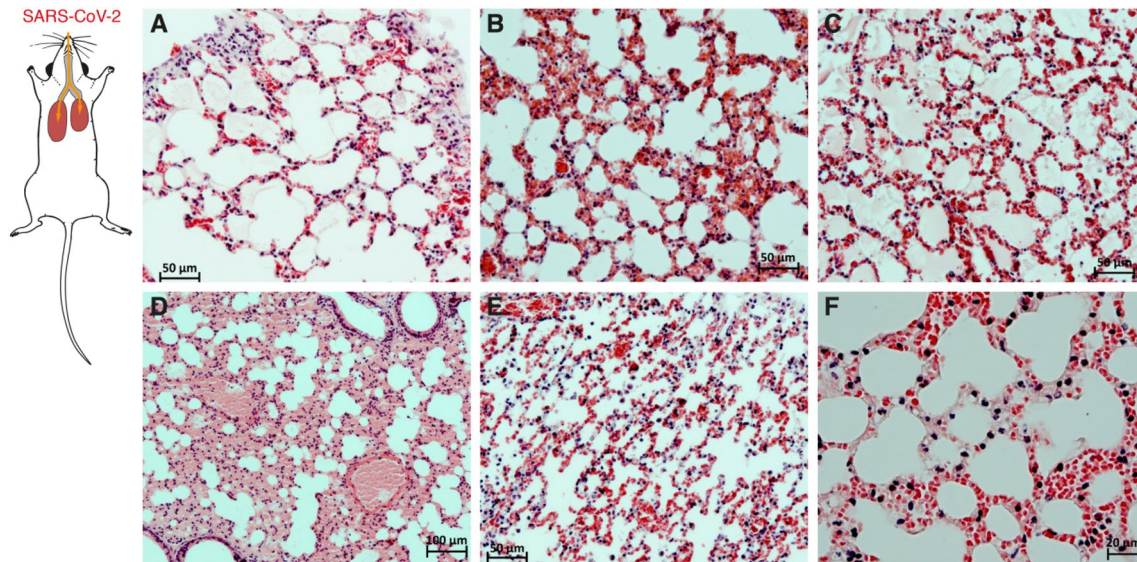

Fig. 6 Fragments of the lungs of male hACE2 mice obtained at autopsy on days 3–4 after intranasal injection of SARS-CoV-2 at a dose of 105–106 PFU: **A**—hyaline-like membranes; **B**—disorders of microcirculation such as congestion, stasis, blood sludge and microthromboses; **C**—tissue detritus in the lumen of pulmonary acini; **D**—transudate in the lumen of acini; **E**—sparse mononuclear cells in the wall and lumen of alveoli; **f**—sparse segmented neutrophils in the alveolar wall. Staining with hematoxylin and eosin. Magnification: 200x (**A**, **B**, **C**, **E**), 100x (**D**), and 400x (**F**)

Table 2 Frequencies of morphological findings in the lungs of mice in noninfectious and infectious models

Morphological findings in the lungs of male mice	Unilateral intrabronchial administration of the GC + LPS mixture, male ICR mice	Infection of male hACE2 mice with SARS-CoV-2
Peribronchial mononuclear/neutrophil infiltration	+ + +	–
Perivascular mononuclear/neutrophil infiltration	+ + +	–
Hyalin-like membranes	–	+ +
Microcirculatory disorders—congestion, stasis, aggregation of red blood cells, and microthromboses	+	+ + +
Transudate in the lumen of pulmonary acini	+ +	+ +
Infiltration of alveolar walls with mononuclear cells / neutrophils	+ + +	+
Infiltration of the alveolar lumen with mononuclear cells/neutrophils	+ + +	+

Sign severity is assessed using semiquantitative scores where "–" means a missing sign, "+" a minimal or mild sign, "+ +" a moderate sign, and "+ + +" a severe sign

7) findings in the lungs because the long-term effects of lung tissue damage are presently unknown due to the early death of animals in the infective model.

Discussion

With the development of the COVID-19 pandemic, the problem of developing new therapies for ARDS, which is a common cause of death in patients with the most severe course of the disease, becomes increasingly urgent [25]. Among patients who received invasive or noninvasive ventilation on the day of ICU admission, the 90-day mortality rate in patients with mild, moderate, and severe ARDS was 30, 34, and 50%, respectively [26].

Development and testing of new therapeutic agents for ARDS begins with verified preclinical data obtained in biological models that reproduce the key aspects of this condition in humans [27–29]. DAD, which is a hallmark of ARDS, is characterized by the appearance of inflammatory infiltration in perivascular and peribronchial areas, with infiltration of the walls and lumen of alveoli, and the filling of pulmonary acini with transudate in the form of unevenly distributed foci [30–32]. The most common model of DAD is intratracheal administration of α-galactosylceramide before the injection of lipopolysaccharide [14, 15]. A serious drawback of this approach is a high animal lethality as the intratracheal administration is associated with damage to both lungs. Another substantial drawback is a requirement of dual intubation of the trachea under general anesthesia, which may make it more difficult to interpret the results obtained in this model due to increased risk of postoperative complications.

A more appropriate approach to generating selective lung damage has been proposed by Paris et al. [18]. The mainstem bronchus was intubated with a thin catheter telescopically guided through a wider catheter intubating the trachea. The authors succeeded in delivering the damaging agent (0.1 N

HCl mixed with a radioactive label) into one lobe of the right lung, and thus were able to track the site and the extent of original lung damage after several days. Because of this "targeted" approach, it was possible to substantially increase the survival of experimental mice as compared to bilateral instillation of 0.1 N HCl [18]. However, hydrochloric acid as an inducer of inflammation has a narrow specificity and may be used for the modeling of severe forms of gastroesophageal reflux (with involvement of bronchopulmonary apparatus) but is not suitable for the modeling of microbiological damage. The intratracheal administration of the damaging agents may lead either to mild damage, with the formation of disparate foci of inflammation, or to very serious damage causing animal death, which excludes the possibility of performing long-term follow-ups [5, 13, 14, 17]. Intrabronchial (unilateral) administration of inducers of inflammation avoids such problems. Pair anatomy of the target organ provides a brilliant opportunity to use the principle of unilaterality in a model of acute lung damage, which enables using the self-contralateral side of the animal as a control while also making possible a long-term follow-up due to the resiliency of the model.

Morphologically, it is known that lung damage is manifested either as DAD or as bronchiolitis obliterans with organizing pneumonia; a combination of these two types of damage is also possible. Lung damage involves epithelium, endothelium, and interstitial tissue of the alveoli. These changes may be extensive (with involvement of both lungs) or local [33, 34]. ARDS is defined as an acute condition that is characterized by a bilateral infiltration of the lungs and severe hypoxemia with no signs of cardiogenic pulmonary edema [35]. Originally, the terms DAD and ARDS were used interchangeably; however, considering the broad interpretation of DAD in practical medicine, this term has been abandoned in clinical practice and instead ARDS is diagnosed based on the following criteria: development of new respiratory symptoms within one week after exposure to a causative factor; bilateral infiltrates found on imaging;

respiratory failure that is not completely explained by other conditions; hypoxemia with PaO2/FiO2 ≤ 300 mm Hg [36]. Thus, our model permits the formation of a unilateral DAD that serves as a morphological substrate of ARDS.

As a biological platform for DAD modeling, we have chosen the left lung. Because the anatomical structure of the left lung involves no division into lobes, variability in the targeted delivery of the inducer is minimized. The model of DAD proposed by us and obtained as described above is characterized by totality. The left lung in its entirety is involved in the process of modeling. The use of antemortem imaging verification of the targeted delivery of the inducer enables exclusion of procedural nonspecificity from the early stages of the experiment.

The parameters of central hemodynamics in the setting of acute lung inflammation are known to undergo a number of specific shifts with an increase of minute blood volume and circulatory volume [37, 38]. Cardiac output often reaches very high values; however, this increase is usually associated with acceleration of cardiac rhythm. In lobar pneumonia, patients demonstrate blood flow acceleration in both systemic and pulmonary circulation, which is likely due to blood bypassing the affected areas of the lungs. During the period of active inflammatory processes, the resistance of systemic vessels in the lungs is decreased, which is considered to be as a result of adaptive reactions of the vasculature to a significant increase in minute blood volume or the exposure of vessel walls to toxic and infective factors. It is evident that a total collapse of the lung tissue of the left lobe in our model unavoidably results in an elevation of blood pressure in the pulmonary circulation and increase of the load, primarily on the myocardium of the right ventricle.

The use of computer tomography of the lungs for intravital evaluation of the extent of damage is widely accepted in the practice of management of patients with pneumonia of any etiology. This method allows the detection of the following radiologic features: focal, diffuse, or extensive (lobar, subtotal, total) increases in the density of pulmonary parenchyma with formation of radiologic patterns of "ground-glass" opacities and alveolar consolidation over the short term, and signs of development of secondary interstitial fibrosis of the lung and areas of atelectasis over the long term. In patients with viral pneumonia secondary to COVID-19 infection, both the density of the lung lobes and volume of damage correlate with disease severity and refine the prognosis [39, 40]. The time course of radiologic features observed in our model allows for intravital detection of the development and resolution of the left-sided lobar pneumonia with simultaneous vicarious hypertrophy in the right lung.

Therefore, a unilateral approach to DAD modeling has been successfully realized in this study. Administration of the mixture of inducers directly into the left bronchus resulted in a complete cutoff of the left lobe from gas exchange, and the pathomorphological pattern observed in the short-term and medium-term periods of follow-up (diffuse alveolar damage of the elements of blood–air barrier combined with signs of microcirculatory disorder) was entirely consistent with the morphological pattern observed in ARDS [15, 22–24].

In a period of long-term follow-up (30–60 d), fibrotic changes were observed in the left lobe of the lung: a moderate peribronchial and perivascular fibrosis, and widening of interalveolar septa of the pulmonary acini. Early morphological findings in myocardium (small foci of necrosis of cardiomyocytes of the right ventricle, dilation of cavities of the right ventricle and right atrium) reflected total atelectasis and cutoff of the left lobe of the lungs from gas exchange; they also indirectly confirmed the development of pulmonary hypertension with an increase of load on the myocardium of the right heart. Subsequently, with the worsening of fibrotic changes in pulmonary parenchyma of the left lobe by the end of a two-month period, a hypertrophy of cardiomyocytes of both right and left ventricles was observed.

According to the results of functional tests, it was found that in the acute and subacute periods of DAP, there is an increase in the respiratory rate, a decrease in the respiratory volume and the peak expiratory flow. These data are in good agreement with the clinical manifestations of ARDS in humans, including coronavirus infection [41, 42].

One of the earliest abnormalities observed in lung injury during ARDS is the elevated levels of the inflammatory cytokines, namely TNF-α, which promote nuclear factor-κB (NF-κB) and histone deacetylase 3 (HDAC-3) nuclear translocation [43]. LPS stimulation initiates a cascade of multiple intracellular signaling events, including NF-κB activation, leading to the release of inflammatory cytokines IL-1β, IL-2, and IL-6, and chemokines MIP-1α/β [44]. Importantly, a recent study, which is in good agreement with our results, indicates that levels of plasma cytokines in human samples with ARDS are similar to those in patients with severe COVID-19 [45]. The development of infectious models in humanized mice hACE2 using live viruses is strictly regulated by biological safety regulations and should be performed in facilities of ABSL-3 level or higher. The number of laboratories and animal facilities where studies on such models can be conducted is very limited. Our data indicate that the current model may be readily applied for studying therapeutic agents that prevent a cytokine storm during ARDS and pathogenesis of the SARS-CoV-2 infection.

WHO has launched a global campaign to test therapeutic agents and vaccines. To achieve this goal, it is important to identify SARS-CoV-2 animal models that provide measurable indicators for testing medical countermeasures [41, 46]. It was shown that while the virus can infect and replicate in numerous animals including ferrets, Syrian hamsters,

and nonhuman primates, infections are largely self-limiting and animals display only minor symptoms [27]. Although such animal models may be very useful in the development of vaccines or antivirals targeting the infection, they can present several hurdles in the monitoring of the course of infection which, in turn, may hinder large investigations [47]. Having analyzed the morphological features of our infectious and noninfectious DAD models provided in Table 2, we conclude that each model has its own unique characteristics.

Similarities and differences between morphological aspects of noninfectious and infectious models of ARDS are attributed to different etiologies of the inflammatory process in the lungs, and none of the existing models is capable of fully reproducing changes observed in the setting of COVID-19 development in humans. Therefore, it is worth using both models for testing the drugs aimed at suppression of the inflammatory process in the lungs, because this would return additional information. Serious limitations on working with infective models also make it necessary to use sterile systems, considering the differences that we have found between the infective models.

An important aspect of ARDS is the cardiopulmonary continuum. At present, we have no long-term data on the morphological changes in the heart and lung of hACE mice that have survived a COVID-19 infection. However, the literature suggests that cardiomegaly with marked dilation of the right ventricle cavity as an overt sign of right heart overload was reported postmortem in patients who had died from COVID-19 infection. Postmortem investigation of myocardium samples has shown focal degenerative changes of cardiomyocytes [42].

Conclusion

We have presented immunological and morphological features of a new experimental noninfectious unilateral model of diffuse alveolar damage of the lungs induced by LPS simultaneously with GC. The model is characterized by 100% animal survival, abrupt increases in plasma levels of cytokines and chemokines, and significant myocardial overload in the right heart with compensatory hypertrophy of cardiomyocytes. The model is "sterile" because it does not need viruses for modeling of severe lung damage and, hence, does not require special conditions for working with viruses. It allows the investigation of potential, innovative therapeutic approaches in a predictable and reproducible model that is close to ARDS with regards to morphological processes occurring in the left lung.

The model is characterized by diffuse homogeneous lesions of the left lung and intact right lung, which ensures the survival of animals and allows us to evaluate not only short-term effects but also long-term changes in the lung tissue associated with organ recovery. The DAD model we have proposed may be widely used for studying the efficacy of candidate molecules for the treatment of infectious respiratory diseases, such as viral pneumonias of different etiology, including SARS-CoV-2.

Declarations

References

1. Potey PM, Rossi AG, Lucas CD, Dorward DA. Neutrophils in the initiation and resolution of acute pulmonary inflammation: understanding biological function and therapeutic potential. J Pathol. 2019;247(5):672–85. https://doi.org/10.1002/path.5221.

2. Gallelli L, Zhang L, Wang T, Fu F. Severe acute lung injury related to covid-19 infection: a review and the possible role for Escin. J Clin Pharmacol. 2020;60(7):815–25. https://doi.org/10.1002/jcph.1644.

3. Li L, Huang Q, Wang DC, Ingbar DH, Wang X. Acute lung injury in patients with COVID-19 infection. Clin Transl Med. 2020;10(1):20–7. https://doi.org/10.1002/ctm2.16.

4. Pfortmueller CA, Spinetti T, Urman RD, Luedi MM, Schefold JC. COVID-19-associated acute respiratory distress syndrome (CARDS): Current knowledge on pathophysiology and ICU treatment—a narrative review. Best Pract Res Clin Anaesthesiol. 2021;35(3):351–68. https://doi.org/10.1016/j.bpa.2020.12.011.

5. Matuschak GM, Lechner AJ. Acute lung injury and the acute respiratory distress syndrome: pathophysiology and treatment. Mo Med. 2010;107(4):252–258. PMCID: PMC6188356

6. Altemeier W.A., Hung C.F., Matute-Bello G. (2017) Mouse Models of Acute Lung Injury. In: Schnapp L., Feghali-Bostwick C. (eds) Acute Lung Injury and Repair. Respiratory Medicine. Humana Press, Cham. https://doi.org/10.1007/978-3-319-46527-2-2.

7. Matthay MA, Howard JP. Progress in modelling acute lung injury in a pre-clinical mouse model. Eur Respir J. 2012;39(5):1062–3. https://doi.org/10.1183/09031936.00204211.

8. Bastarache JA, Blackwell TS. Development of animal models for the acute respiratory distress syndrome. Dis Model Mech. 2009;2:218–23. https://doi.org/10.1242/dmm.001677.

9. Matute-Bello G, Downey G, Moore BB, et al. An official American Thoracic Society workshop report: features and measurements of experimental acute lung injury in animals. Am J Respir Cell Mol Biol. 2011;44:725–38. https://doi.org/10.1165/rcmb.2009-0210ST.

10. Yehya N. Lessons learned in acute respiratory distress syndrome from the animal laboratory. Ann Transl Med. 2019;7(19):503. https://doi.org/10.21037/atm.2019.09.33.

11. Ashbaugh DG, Bigelow DB, Petty TL, Levine BE. Acute respiratory distress in adults. Lancet. 1967;2(7511):319–23 (**PMID: 16548822**).

12. Nieman GF, Al-Khalisy H, Kollisch-Singule M, et al. A Physiologically Informed Strategy to Effectively Open, Stabilize, and Protect the Acutely Injured Lung. Front Physiol. 2020; 11:227. Published 2020 Mar 19. https://doi.org/10.3389/fphys.2020.00227.

13. Matute-Bello G, Frevert CW, Martin TR. Animal models of acute lung injury. Am J Physiol Lung Cell Mol Physiol. 2008;295(3):L379–99. https://doi.org/10.1152/ajplung.00010.2008.

14. Aoyagi T, Yamamoto N, Hatta M, Tanno D, Miyazato A, Ishii K, et al. Activation of pulmonary invariant NKT cells leads to exacerbation of acute lung injury caused by LPS through local production of IFN-γ and TNF-α by Gr-1+ monocytes. Int Immunol. 2011;23(2):97–108. https://doi.org/10.1093/intimm/dxq460.

15. Pomytkin I.A., Karkischenko V.N., Fokin Yu.V., Nesterov M.S., Petrova N.V. A Model of Fatal Acute Lung Injury and Acute Respiratory Distress Syndrome. Journal Biomed. 2020;16(4):24–33. (In Russ.) https://doi.org/10.33647/2074-5982-16-4-24-33.

16. D'Alessio FR. Mouse models of acute lung injury and ARDS. Methods Mol Biol. 2018;1809:341–50. https://doi.org/10.1007/978-1-4939-8570-8_22.

17. Kudo D, Toyama M, Aoyagi T, Akahori Y, Yamamoto H, Ishii K, et al. Involvement of high mobility group box 1 and the therapeutic effect of recombinant thrombomodulin in a mouse model of severe acute respiratory distress syndrome. Clin Exp Immunol. 2013;173(2):276–87. https://doi.org/10.1111/cei.12106.

18. Paris AJ, Guo L, Dai N, Katzen JB, Patel PN, Worthen GS, Brenner JS. Using selective lung injury to improve murine models of spatially heterogeneous lung diseases. PLoS ONE. 2019;14(4): e0202456. https://doi.org/10.1371/journal.pone.0202456.

19. Zacharias WJ, Frank DB, Zepp JA, Morley MP, Alkhaleel FA, Kong J, et al. Regeneration of the lung alveolus by an evolutionarily conserved epithelial progenitor. Nature. 2018;555(7695):251–5. https://doi.org/10.1038/nature25786.

20. Villar J, Zhang H, Slutsky AS. Lung repair and regeneration in ARDS: role of PECAM1 and Wnt signaling. Chest. 2019;155(3):587–94. https://doi.org/10.1016/j.chest.2018.10.022.

21. Loginova SYA, Shchukina VN, Savenko SV, Borisevich SV. Antiviral activity of Kagocel® in vitro against virus SARS-CoV-2. Antibiot Chemother. 2020;65:3–4. https://doi.org/10.37489/0235.2990.2020.65.3.4.3.6.

22. Hanley B, Lucas SB, Youd E, Swift B, Osborn M. Autopsy in suspected COVID-19 cases. J Clin Pathol. 2020;73(5):239–42. https://doi.org/10.1136/jclinpath-2020-206522.

23. Sun SH, Chen Q, Gu HJ, et al. A mouse model of SARS-CoV-2 infection and pathogenesis. Cell Host Microbe. 2020;28(1):124-133.e4. https://doi.org/10.1016/j.chom.2020.05.020.

24. Hong W, Yang J, Bi Z, et al. A mouse model for SARS-CoV-2-induced acute respiratory distress syndrome. Signal Transduct Target Ther. 2021;6(1):1. https://doi.org/10.1038/s41392-020-00451-w.

25. Aeffner F, Bolon B, Davis IC. Mouse models of acute respiratory distress syndrome: a review of analytical approaches, pathologic features, and common measurements. Toxicol Pathol. 2015;43(8):1074–92. https://doi.org/10.1177/0192623315598399.

26. COVID-ICU Group on behalf of the REVA Network and the COVID-ICU Investigators. Clinical characteristics and day-90 outcomes of 4244 critically ill adults with COVID-19: a prospective cohort study. Intensive Care Med. 2021 47(1):60–73. doi: https://doi.org/10.1007/s00134-020-06294-x.

27. Muñoz-Fontela C, Dowling WE, Funnell SGP, et al. Animal models for COVID-19. Nature. 2020;586:509–15. https://doi.org/10.1038/s41586-020-2787-6.

28. Brenner JS, Bhamidipati K, Glassman P, Ramakrishnan N, Jiang D, Paris AJ, et al. Mechanisms that determine nanocarrier targeting to healthy versus inflamed lung regions. Nanomedicine. 2017. https://doi.org/10.1016/j.nano.2016.12.019.

29. Vlahos R, Bozinovski S. Recent advances in pre-clinical mouse models of COPD. Clin Sci (Lond). 2014;126(4):253–65. https://doi.org/10.1042/CS20130182.

30. Thompson BT, Chambers RC, Liu KD. Acute respiratory distress syndrome. N Engl J Med. 2017;377(19):1904–5. https://doi.org/10.1056/NEJMc1711824 (**PMID: 29117492**).

31. Bernard G. Acute lung failure—Our evolving understanding of ARDS. N Engl J Med. 2017;377(6):507–9. https://doi.org/10.1056/NEJMp1706595 (**PMID:28792872**).

32. Cardinal-Fernández P, Lorente JA, Ballén-Barragán A, Matute-Bello G. Acute Respiratory Distress Syndrome and Diffuse Alveolar Damage. New Insights on a Complex Relationship. Ann Am Thorac Soc. 2017 Jun;14(6):844–850. https://doi.org/10.1513/AnnalsATS.201609-728PS.

33. Yardy A, Tomashefski I, Yagan R, Klienerman I (1989) Regional alveolar damage (RAD). A localized counterpart of diffuse alveolar damage. Am. J. Clin. Pathol. 92: 10.

34. Chernyaev AL, Samsonova MV (2005) The etiology, pathogenesis, and pathological anatomy of diffuse alveolar lesion. General Reanimatol. 1(5):13–16. (In Russ.) https://doi.org/10.15360/1813-9779-2005-5-13-16.

35. Bernard GR, Artigas A, Brigham KL, Carlet J, Falke K, Hudson L, Lamy M, Legall JR, Morris A, Spragg R (1994) The American-European Consensus Conference on ARDS. Definitions, mechanisms, relevant outcomes, and clinical trial coordination. Am J Respir Crit Care Med. Mar;149(3 Pt 1):818–24. doi: https://doi.org/10.1164/ajrccm.149.3.7509706.

36. Ranieri VM, Rubenfeld GD, Thompson BT, Ferguson ND, Caldwell E, Fan E, Camporota L, Slutsky AS (2012) ARDS Definition Task Force. Acute respiratory distress syndrome: the Berlin Definition. JAMA. 307(23):2526–33.

37. Toth I, Leiner T, Mikor A, Szakmany T, Bogar L, Molnar Z. Hemodynamic and respiratory changes during lung recruitment and descending optimal positive end-expiratory pressure titration in patients with acute respiratory distress syndrome. Crit Care Med. 2007;35(3):787–93. https://doi.org/10.1097/01.CCM.0000257330.54882.BE.

38. Cortes-Puentes GA, Oeckler RA, Marini JJ. Physiology-guided management of hemodynamics in acute respiratory distress syndrome. Ann Transl Med. 2018;6(18):353. https://doi.org/10.21037/atm.2018.04.40.

39. Lyu P, Liu X, Zhang R, Shi L, Gao J. The performance of chest CT in evaluating the clinical severity of COVID-19 pneumonia: identifying critical cases based on CT characteristics. Invest Radiol. 2020;55(7):412–21. https://doi.org/10.1097/RLI.0000000000000689.

40. Shen C, Yu N, Cai S, Zhou J, Sheng J, Liu K, Zhou H, Guo Y, Niu G. Quantitative computed tomography analysis for stratifying the severity of Coronavirus Disease 2019. J Pharmaceutical Anal. 2020. https://doi.org/10.1016/j.jpha.2020.03.004.

41. Bauer DC et al. Supporting pandemic response using genomics and bioinformatics: A case study on the emergent SARS-CoV-2 outbreak. Transbound Emerg Dis 24, https://doi.org/10.1111/tbed.13588

42. Fox SE, Akmatbekov A, Harbert JL, Li G, Quincy Brown J, Vander Heide RS. Pulmonary and cardiac pathology in African American patients with COVID-19: an autopsy series from New Orleans. Lancet Respir Med. 2020;8(7):681–6. https://doi.org/10.1016/S2213-2600(20)30243-5.

43. Pooladanda V, Thatikonda S, Bale S, Pattnaik B, Sigalapalli DK, Bathini NB, Singh SB, Godugu C. Nimbolide protects against endotoxin-induced acute respiratory distress syndrome by inhibiting TNF-α mediated NF-κB and HDAC-3 nuclear

translocation. Cell Death Dis. 2019;10(2):81. https://doi.org/10.1038/s41419-018-1247-9.

44. Ramana KV et al. (2006) Aldose reductase mediates the lipopolysaccharide-induced release of inflammatory mediators in RAW264.7 murine macrophages. J Biol Chem 281: 33019–33029 https://doi.org/10.1074/jbc.M603819200.

45. Wilson JG, Simpson LJ, Ferreira AM, Rustagi A, Roque J, Asuni A, Ranganath T, Grant PM, Subramanian A, Rosenberg-Hasson Y, Maecker HT, Holmes SP, Levitt JE, Blish CA, Rogers AJ. Cytokine profile in plasma of severe COVID-19 does not differ from ARDS and sepsis. JCI Insight. 2020;5(17): e140289. https://doi.org/10.1172/jci.insight.140289.

46. Hodgson J The pandemic pipeline. Nature biotechnology 38, 523–532 (2020). DOI: https://doi.org/10.1038/d41587-020-00005-z

47. Gantier MP. Animal models of COVID-19 hyper-inflammation. Respirology. 2021;26(3):222–4. https://doi.org/10.1111/resp.13997.